Available online at www.sciencedirect.com
ScienceDirect
Trans. Nonferrous Met. Soc. China 32(2022) 1261−1276
Transactions of Nonferrous Metals Society of China
www.tnmsc.cn

Microscale deformation behavior of sandstone mineral particles based on XCT scanning

Ya-guang QIN[1,2], De-sheng GU[2], Jian-hua HU[2], Dong-jie YANG[2], Shao-wei MA[2], Xin BAI[3], Chun-di FENG[2]

1. Power China Huadong Engineering Corporation Limited, Hangzhou 311122, China;
2. School of Resources and Safety Engineering, Central South University, Changsha 410083, China;
3. School of Resources Environment and Safety Engineering, University of South China, Hengyang 421000, China

Received 29 October 2020; accepted 24 December 2021

Abstract: This work aimed to quantify the physical and mechanical behavior of three-dimensional microstructures in rocks under uniaxial compression. A high-precision in situ XCT (X-ray transmission computed tomography) technology was applied to investigating the behavior of mineral grains in sandstone: the movement, the rotation deformation, and the principal strains between fault zone and non-fault zone. The results indicate that after unloading, the shear strain of mineral grains is periodic in the radial direction, the strain of mineral grains in the fracture zone is about 30 times of the macro strain of the specimen, which is about 5 times in the non-fracture zone, and the shear strain near the fault zone is larger than the compressive strain, and there is the shear stress concentration feature.
Key words: grain deformation; in situ XCT; failure behavior; Stokes rotation; material line

1 Introduction

The physical and mechanical behaviors of rocks are determined by the deformation behavior [1,2], the contact behavior [3] and the interaction relationship of rock components (pores, grains, fractures, and cement) [4−7]. The contact [8] and friction [9] phenomena between mineral grains are related to the formation, evolution, and propagation mechanism of seismic wave [10], and the geometric features of mineral grains affect the crack propagation [11]. The standard principle of local symmetry [12,13] and the strain-energy density criterion [14] are usually applied to explaining the repulsive cracks [15], with the geometric conditions remaining lacking. However, LIANG et al [16] investigated the deformation of mineral grains and the crack propagation path of rocks. The results showed that there is a geometric correlation between the crack path deflection and the motion of mineral grains. In addition, the deformation, the movement behaviors, and the stress evolution of mineral grains directly reflect the formation and evolution of local deformation zones and the propagation and expansion of cracks [17−21]. Therefore, the geometric properties and movement behaviors of mineral grains are the key factors for assessing the stability of rock mass engineering.

Due to the technical limitations, research on the physical and mechanical properties of mineral grains mainly focused on numerical simulations and two-dimensional laboratory experiments on the surface of materials. KOCK and HUHN [22], and LIU et al [23] made simulation by discrete element method (DEM) to identify the effects of mineral grains with different shapes and sizes under uniaxial compression on deformation, strength (crack initiation strength, damage strength and peak

Corresponding author: Jian-hua HU, Tel: +86-13787056402, E-mail: hujh21@csu.edu.cn;
Dong-jie YANG, Tel: +86-18684911183, E-mail: yangdjxx@csu.edu.cn
DOI: 10.1016/S1003-6326(22)65872-2

strength) of rocks, and investigate the friction properties between mineral grains. LIANG et al [16] studied the rock crack propagation path and mineral grain migration under the condition of medium and low strain rate loading by scanning electron microscopy (SEM), and analyzed the fine granulation and flow properties of mineral grains. SUNDARAM and TIPPUR [24] studied the deformation characteristics of granular matter around precracked solids under dynamic loading by digital image correlation (DIC) technology and obtained dynamic propagation patterns of different precracks. TAN et al [25] indirectly obtained the interface separation characteristics of two-dimensional plane grains by digital speckle techniques and micromechanics theory. Based on the results, a cohesive law at the microscopic scale was established, and the cohesive strength and softening modulus of the interfaces were analyzed. MARUYAMA and HIRAGA [26] used the marker lines to investigate the rotation and deformation properties of mineral grains on rock surfaces. The results showed that grain boundary slides (GBSs)-induced grain rotation and crystallographic preferred orientation (CPO) behavior affect the seismic properties of the Earth's mantle. The stratum response characteristics and creep mechanism of the upper mantle during earthquakes were further revealed. At the same time, DONG et al [27] found that the superplastic deformation behavior of feldspar and quartz reflects the deformation mechanism of the mantle on Earth. Therefore, the grain-scale microstructure controls the macroscopic fracture patterns. The rock fracture phenomena have a strong correlation with the plastic behaviors of the material microstructure, which affect the macroscopic strength of rocks [20,28].

The deformation and kinematic characteristics of mineral grains have a strong correlation with rock fracture and rock mass strength. However, the above research lacked a complete three-dimensional characterization of the physical and mechanical properties of mineral grains. There were some errors caused by the out-of-plane displacement of mineral grains. Therefore, based on the X-ray computed tomography (XCT) technique, we identified the deformation, movement, rotation, and stress state of mineral grains after unloading. The differences of the physical and mechanical behaviors of mineral grains in the fracture and non-fracture zones of rocks were investigated. A material line was constructed based on rational mechanics theory, and the shear strain of CT slices was calculated by measuring the local rotation angle. The relationship between rock crack propagation and grain movement was studied.

2 Experimental

Based on the in situ XCT technique, which is a nondestructive testing method, the three-dimensional strain and stress state of mineral grains in rock were measured. Compared with other methods, the in situ XCT method can always maintain a constant loading stress during scanning and maintain the original internal structure of the rock to the greatest extent, which avoids changes in the internal structure of the rock caused by stress unloading. At the same time, the high-precision CT scanning can accurately obtain the 3D shapes of mineral grains in the rock without destroying the original state of the rock.

The samples of poorly cemented sandstone, without removing any water to maintain the microstructure, were collected from Yunnan Province in China. The particle size of mineral grains of sandstone was approximately 0.1 mm. The samples (d3.8 mm × 7.4 mm) were extracted from a sandstone core (d50 mm × 100 mm) by a focused ion beam (FIB), which eliminated the end effects. The mineral powder was analyzed by XRD diffraction and contained quartz, muscovite, calcite, albite, and hematite, as shown in Fig. 1. The density, elastic modulus, and Poisson's ratio of the mineral components are shown in Table 1.

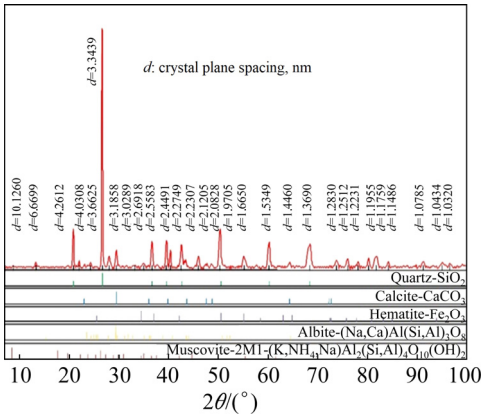

Fig. 1 XRD patterns of sandstone samples showing characteristic peaks of different minerals

Table 1 Modulus and density of common minerals in sandstone

Mineral	Elastic modulus/GPa	Density/ ($g \cdot mm^{-3}$)	Poisson's ratio
Quartz	94.5	2.65	0.08
Muscovite	56.8	2.81	0.25
Calcite	84.1	2.75	0.32
Albite	88.1	2.61	0.26
Hematite	211.7	4.4	0.15

The test was conducted with the Xradia 520 Versa (XCT) and Material Testing Stage (MTS) with a servo control system. The accuracies of the displacement and the load measurements are ±0.01 mm and ±8 N, respectively. The maximum spatial resolution of XCT can reach 700 nm. The testing process is as follows.

(1) The sandstone in the natural state was cut into a cylinder by FIB, and the upper and lower end surfaces of the sample were polished to eliminate friction. Preservative film was used to wrap the samples to maintain the integrity of the samples after unloading.

(2) The XCT and MTS experimental devices and systems were adjusted, and sandstone was scanned for the first time. The sample was loaded with a displacement control mode at a rate of 0.003 mm/min.

(3) After unloading, the sample was scanned for the second time, during which sandstone was shot every 0.2° and uniformly rotated from 180° to −180°, and 1800 projections were taken from different angular views.

(4) 3D reconstruction of the projected data before loading and after unloading was carried out to obtain the 3D structure of its internal components, and the nonlocal means algorithm was adopted to filter the images [29].

(5) The denoised image was automatically segmented by a watershed algorithm [30] using Amira software, and pixels of the mineral grains were extracted for 3D reconstruction.

(6) The deformation, stress and strain of mineral grains were calculated by using a deformation gradient.

Figure 2 shows the typical images before and after uniaxial compression. Six groups of samples were tested. The average axial strain was 0.013, the compressive strength of rock under uniaxial compression was 30 MPa, and the elastic modulus was 0.23 GPa.

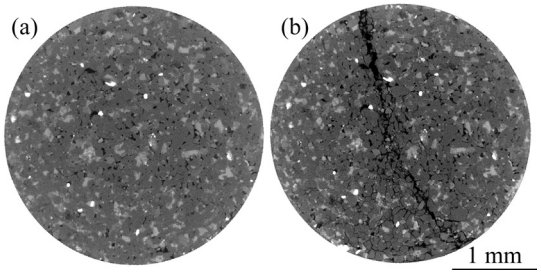

Fig. 2 In situ XCT images of sandstone: (a) Before loading; (b) After unloading

3 Results

3.1 Deformation behaivor

To identify the movement, rotation, strain and stress of mineral grains, the radial distribution function (RDF) [31] and equivalent diameter [32] of hematite grains were calculated. To ensure the accuracy of calculation results, the contact ratio of the grains before and after uniaxial compression was obtained based on the radial distribution function of CT images and the movements of the grains. The bounding box algorithm was applied to extracting the principal axes and volume of each pair of mineral grains and to characterize the changes of volume. Then, the deformation behavior of mineral grains was analyzed based on the changes of volume and principal axes.

The RDF is typically used to describe grain correlations in granular systems and to acquire the order of mineral components to characterize the disorder degree of the three-dimensional structure of mineral grains after compression. For specified three-dimensional coordinates of mineral grains, the RDF can be used to calculate their coordinates after compression and compute their probability distribution. The RDF, $g(r)$, is computed as follows:

$$g(r)=\frac{1}{\rho_0}\frac{n(r)}{V}\approx\frac{1}{\rho_0}\frac{n(r)}{4\pi r^2\Delta r} \tag{1}$$

where $n(r)$ is the radius of mineral grains from r to $r+\Delta r$, V is the volume of mineral grains, and ρ_0 is the density of mineral grains.

The equivalent radius R was applied to calculating the RDF because the grains have complex shapes, and their irregularity makes it difficult to compute the RDF. The equivalent radius

R can be obtained as follows:

$$R=(6V/\pi)^{1/3} \quad (2)$$

We then obtained the movements of mineral grains by calculating the changes in the center of mass of the grains before and after compression. The ID number for each grain can be assigned. Finally, the bounding box algorithm was adopted to estimate the volume changes of the grains before and after compression. The boxes surrounded by them are L_1, L_2 and L_3, where L_1, L_2 and L_3 represent the minimum, intermediate and maximum axis lengths of the box, respectively.

Figure 3 shows variation of the probability distribution with the incremental volume of mineral grains. In general, the volume of most mineral grains increased, but that of some grains decreased. According to Eq. (2), the maximum diameter of the grains is 0.3 mm. This grain with the maximum diameter was then placed in the sample center and used to calculate the probability distribution of the contact ratio of mineral grains in the period of R_N (N= 1, 2, 3).

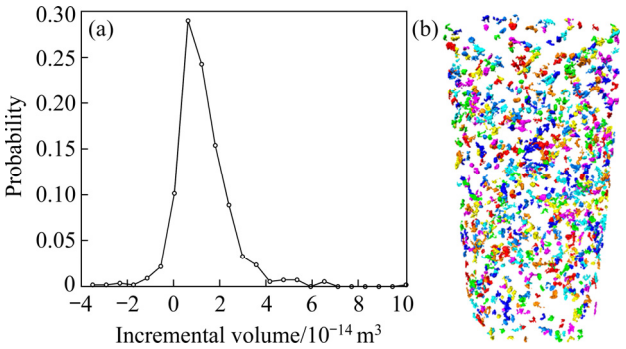

Fig. 3 Probability distribution varying with incremental volume of grains (a) and distribution of mineral grains after unloading (b)

Figure 4 shows that the $g(r)$ of this grain with maximum diameter equals 1. The $g(r)$ values of the rest of the grains are less than 0.0769, showing that there is no contact among the mineral grains. Therefore, the tracking results of the grains before and after compression are reliable.

Figure 5 shows the results of the bounding box. The compactness was considered in the bounding box algorithm to ensure the authenticity and reliability of the results.

In Fig. 5(a), the curves of L_3/L_2 before and after compression are similar in shape. The results mean that after uniaxial compression, mineral

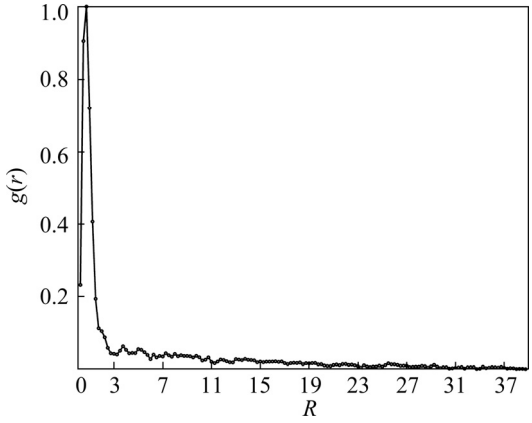

Fig. 4 Variation of normalized radial distribution function $g(r)$ with equivalent radius R

grains have the same change trend (i.e., increase or decrease simultaneously) or remain unchanged about the lengths of the maximum axis and the second major axis. According to Fig. 5(d), the overall volume of mineral grains increases after compression. Therefore, the lengths of mineral grains, L_3 and L_2, increase simultaneously.

In Fig. 5(b), the value of L_2/L_1 after compression jumps between 3 and 5 compared with that before compression, and the fluctuation between 3.5 and 3.8 shows an increasing trend, followed by a decreasing trend, and gradually approaches the curve before compression. Therefore, after compression, the volume of mineral grains mainly shows an increasing trend, the length of the L_3 axis of mineral grains changed greatly, which is consistent with Fig. 5(b), and the fluctuation gradually decreases, which is consistent with Fig. 5(c). The experimental results in Figs. 5(a−c) are mutually verified. In addition, the volume change of mineral grains after compression may change the sphericity of the grains, so the change in grain shape will lead to a change in contact area and contact relationship among the grains, thus leading to a change in friction properties among the grains.

Furthermore, the sphericity of mineral grains was analyzed, and the sphericity was computed by $(36\pi V^2/S^3)^{1/3}$, where S is the surface area of the grains. The sphericity of the mineral grains before and after compression is 0.27−0.993 and 0.333−0.994, respectively. The mean (μ) and variance (σ^2) of the sphericity before and after compression are μ=0.730, σ^2=0.152 and μ=0.766, σ^2=0.135, respectively. More than 95% of volume

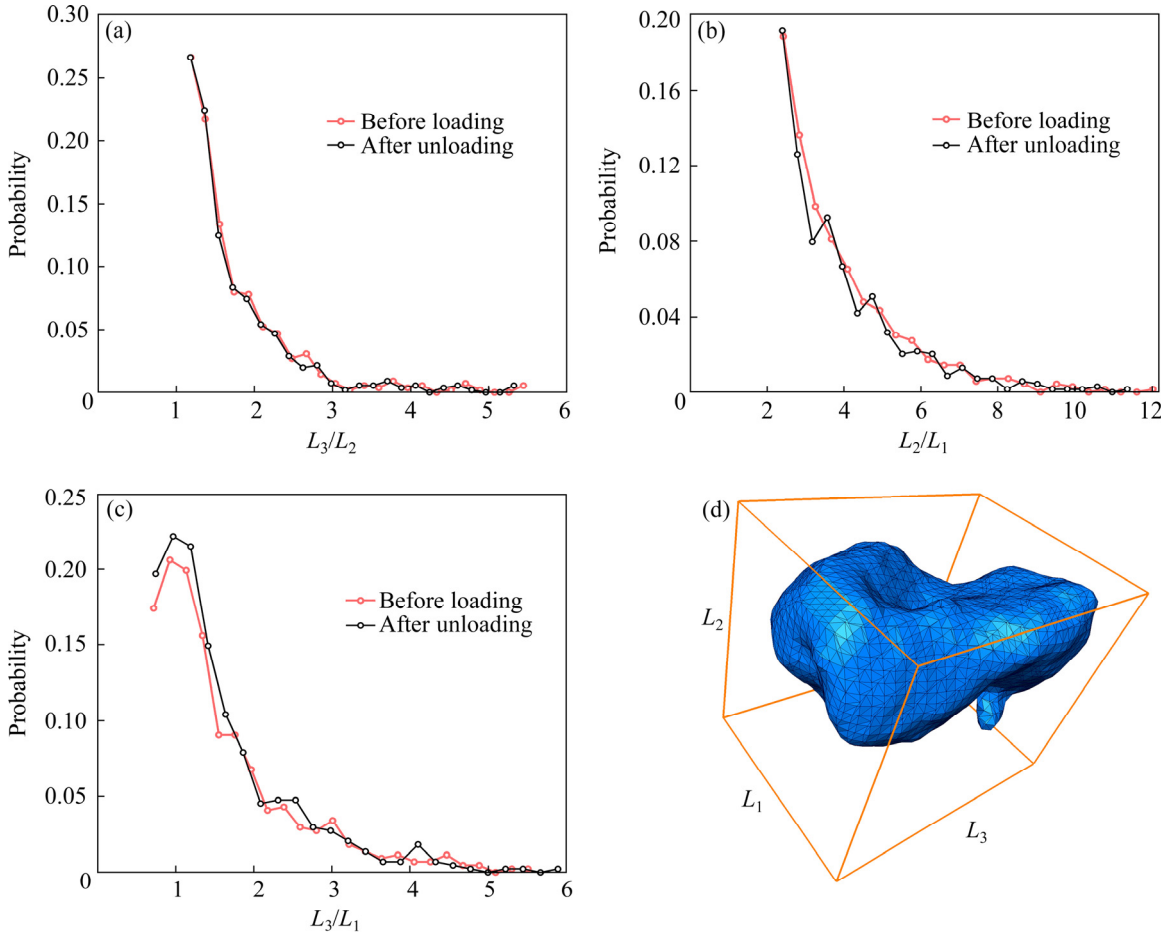

Fig. 5 Probability distributions of L_3/L_2 (a), L_2/L_1 (b), and L_3/L_1 (c) before loading and after unloading, and bounding box (d)

increment of the grains is mainly concentrated in the range of $0-3\times10^{-14}$ m^3, as shown in Fig. 3. Therefore, from a statistical perspective, as the lengths of the L_3 and L_2 axes of some mineral grains increase, the length of the L_1 axis increases, resulting in the sphericity of most mineral grains increasing.

3.2 Translation and rotation

3.2.1 Computational method for mineral grain translation and rotation

In order to extract the displacement of each pair of mineral grains, the grains before and after compression were placed in the same coordinate system. Firstly, the first-order moments were applied to calculating the centroid of the grains to obtain their spatial position. Secondly, the centroid displacement before and after compression was calculated by using the distance formula between two points in geometry. Then, the probability distribution of the total displacement of grains was calculated, and the second-order moments were applied to obtaining the covariance matrix, $\boldsymbol{A}$, computed as follows:

$$\boldsymbol{A}=\begin{bmatrix} \frac{1}{A(x)}\int_x x\mathrm{d}x\mathrm{d}y\mathrm{d}z & \frac{1}{A(x)}\int_x (x-M_{1x})(y-M_{1y})\mathrm{d}x\mathrm{d}y\mathrm{d}z & \frac{1}{A(x)}\int_x (x-M_{1x})(z-M_{1z})\mathrm{d}x\mathrm{d}y\mathrm{d}z \\ \frac{1}{A(x)}\int_x (x-M_{1x})(y-M_{1y})\mathrm{d}x\mathrm{d}y\mathrm{d}z & \frac{1}{A(x)}\int_y x\mathrm{d}x\mathrm{d}y\mathrm{d}z & \frac{1}{A(x)}\int_x (y-M_{1y})(z-M_{1z})\mathrm{d}x\mathrm{d}y\mathrm{d}z \\ \frac{1}{A(x)}\int_x (x-M_{1x})(z-M_{1z})\mathrm{d}x\mathrm{d}y\mathrm{d}z & \frac{1}{A(x)}\int_x (y-M_{1y})(z-M_{1z})\mathrm{d}x\mathrm{d}y\mathrm{d}z & \frac{1}{A(x)}\int_z x\mathrm{d}x\mathrm{d}y\mathrm{d}z \end{bmatrix} \tag{3}$$

where $A(x)$ is the function of spatial position, and M is the second-order moments.

For the symmetric matrix in Eq. (3), the maximum, second and minimum eigenvalues of mineral grains were computed by normal vector decomposition [33]. Finally, the translation and rotation of 689 grains were analyzed. The density change of mineral grains in the process of movement was ignored. It is assumed that the grain density is uniform before and after the movement. Therefore, the centroid of mineral grains is equivalent to the center of mass.

3.2.2 Results analysis for mineral grain translation and rotation

Figure 6 shows the displacement distribution of mineral grains before and after compression. In Fig. 6(a), the straight lines represent the displacement of each pair of grains. We can see the position of mineral grains before and after compression, and the movement of mineral grains mainly presents the overall sinking trend, while the opposite movement phenomenon appears in the local area. Figure 6(b) shows the probability distribution of displacement of mineral grains after compression. The displacement of mineral grains was mainly distributed between 0.035 and 0.2 mm, among which the displacement of 22% mineral grains was concentrated at 0.06 mm and the displacement of 13% mineral grains was concentrated between 0.13 and 0.14 mm.

According to Eq. (1), the spatial distribution of mineral grains is discrete, and the displacement of each mineral grain is less than the distance between any two mineral grains, as shown in Fig. 7(a). The number of grains at different normalized heights, as shown in Table 2, was 227 in the height range of 0.6−0.8. The minimum number of grains was 70 in the height range of 0.8−1.0.

The distribution of 689 mineral grains in Fig. 7(a) on the normalized height of the x-axis was analyzed. Table 2 shows the number of mineral grains located at each normalized height in Fig. 7(b). Obviously, the number of mineral grains at the top position of the sandstone is smaller than that at other positions. Due to the insufficient number of samples at the top of the sample, the accuracy of the results may be low, and the error of the calculation results cannot be specifically estimated.

Figure 7(c) shows that mineral grains experienced the most total displacement at the top of the sandstone. Figures 7(a) and (b) show that most displacements in the horizontal plane occurred on the side of the sandstone, and the displacements of the x and y axes were highly symmetrical. The radial displacement near the central axis is smaller, while the displacement far from the central axis is larger. This is due to the transverse expansion of the sandstone during compression, so the cumulative displacement of the grains far away from the central axis is larger.

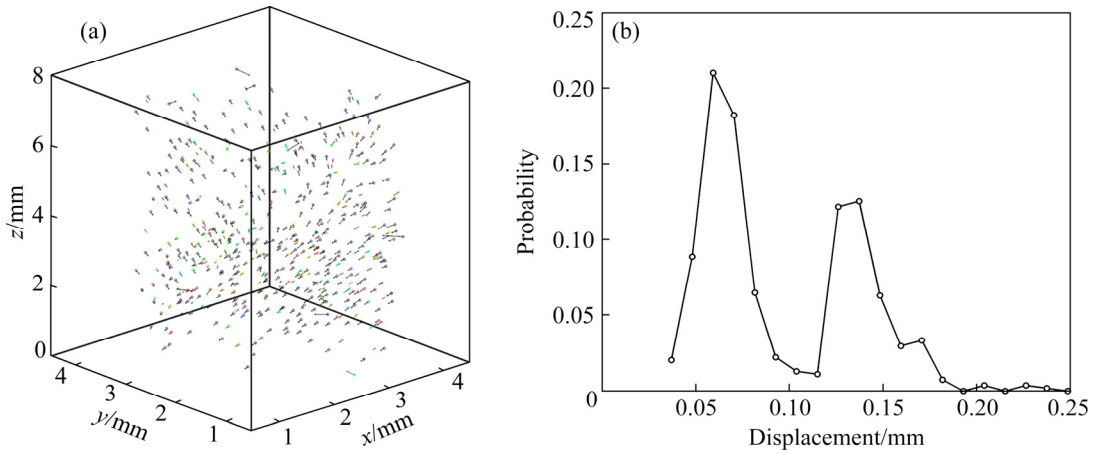

Fig. 6 Displacement for each pair of grains (a) and probability distribution of total displacement for grains (b)

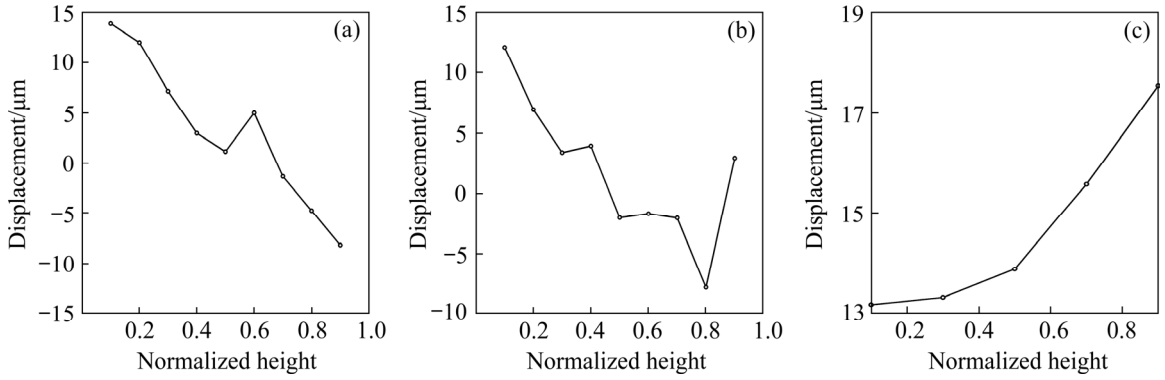

Fig. 7 Average total displacement versus normalized height in x (a), y (b) and z (c) axes

Table 2 Numbers of mineral grains at different normalized heights

Normalized height	0−0.2	0.2−0.4	0.4−0.6	0.6−0.8	0.8−1.0
Number of mineral grains	73	178	141	227	70

The rotation angles of grains are shown in Fig. 8(a), and Fig. 8(b) shows the average rotation of mineral grains as a function of normalized height. As shown in Fig. 8(b), the average incremental angle of the grains decreases with increasing height, and the maximum value appears at the height of 0.7. The change in the average incremental angle of the upper sandstone is larger than that of the lower sandstone, which may be caused by the large friction value of the lower sample. Therefore, as the height increases, the rotation angle of the mineral grains tends to increase along the loading direction.

3.3 Normal strain and stress calculation and statistical analysis of mineral grains

3.3.1 Stress and strain computational method for mineral grains

The approximating irregular grain shapes by ellipsoid is a practical way to evaluate the effective properties of mineral grains. We computed the covariance matrix and eigenvalues for tracked grains before and after compression as described in Section 3.2. By applying normal vector decomposition, this symmetric matrix can be described as $\boldsymbol{C}=\boldsymbol{Q}\,\boldsymbol{\Lambda}\,\boldsymbol{Q}$, where $\boldsymbol{Q}$ represents the eigenvector matrix and $\boldsymbol{\Lambda}$ represents the eigenvalue matrix, which can be used to describe three axes of each grain [33]. Then, before deformation, the grain is expressed as

$$\boldsymbol{A}_j^{0i}\boldsymbol{e}_i = \boldsymbol{E}_j \tag{4}$$

After deformation, the grain is expressed as

$$\boldsymbol{A}_j^{i}\boldsymbol{e}_i = \boldsymbol{E}_j \tag{5}$$

where $\boldsymbol{e}_i$ is a unit vector, $\boldsymbol{A}_j^{0i}$ and $\boldsymbol{A}_j^{i}$ represent the transformation matrices of each pair of grains before loading and after unloading, and $\boldsymbol{E}_j$ is the eigenvalue of the grain. Then, we compute the deformation tensor, $\boldsymbol{F}_j^{i}$, as follows:

$$\boldsymbol{A}_j^{i} = \boldsymbol{F}_j^{i}\boldsymbol{A}_l^{0i} \tag{6}$$

The strain $\boldsymbol{\varepsilon}_j^{i}$ and stress $\boldsymbol{\sigma}_{ij}$ tensors, are represented as follows:

$$\boldsymbol{\varepsilon}_j^{i} = \boldsymbol{F}_j^{i} - \boldsymbol{\delta}_j^{i} \tag{7}$$

$$\boldsymbol{\sigma}_{ij} = \lambda\varepsilon_{ll}\delta_{ij} + 2\mu\varepsilon_{ij} \tag{8}$$

where $\boldsymbol{\delta}$ is the Kronecker symbol, ε_{ll} is the strain in principal axes, $\lambda(=E\upsilon/[(1+\upsilon)(1-2\upsilon)])$ and $\mu(=E/[2(1+\upsilon)])$ are Lame constants, and E and υ are the elastic modulus and Poisson's ratio, respectively.

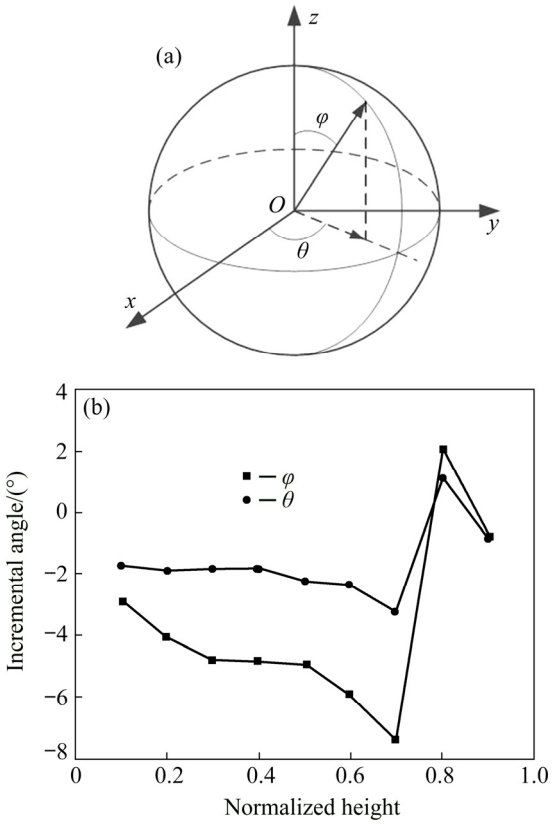

Fig. 8 Rotation angles of grains (a) and incremental angles of mineral grains as function of normalized height (b)

3.3.2 Stress and strain distribution of mineral grains

Figure 9 illustrates after compression the average stress and strain components of mineral grains as a function of normalized height, $(h-z)/h$, where h is the height of the sandstone and z is the z coordinate of the grain centroid. On the whole, the curves of the principal components of the strain and stress of the grains are consistent in shape.

In Fig. 9(a), the strain components of mineral grains ε_{xx}, ε_{yy} and ε_{zz} change in the ranges of 0.02−0.04, 0.01−0.04 and −0.03−0.11, respectively. The fluctuation of the strain component ε_{zz} is the most significant, and the fluctuation of the strain component ε_{xx} is the least significant. The strain components of the mineral grains, ε_{xx} and ε_{yy}, fluctuated in the range of 0.01−0.04, showing a

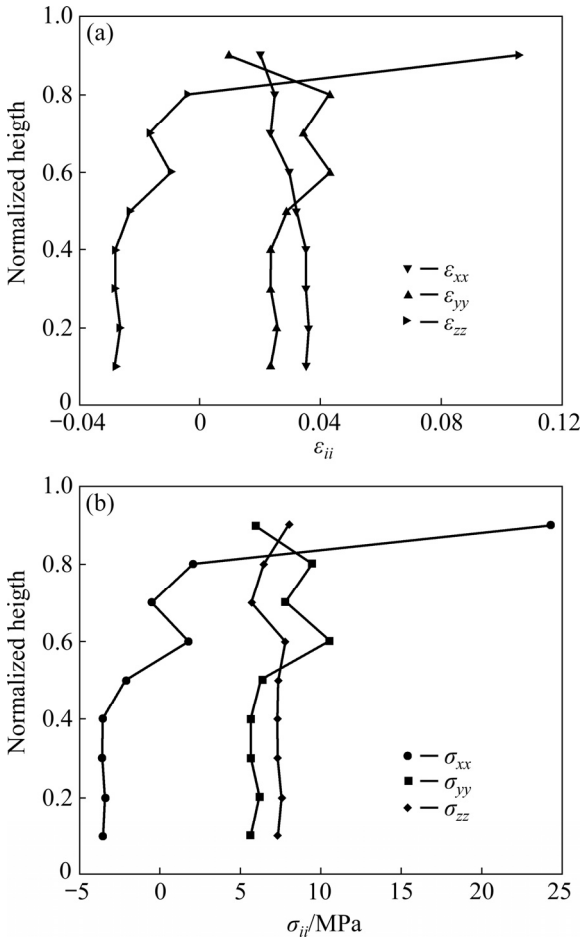

Fig. 9 Average strain (a) and stress (b) of grains as function of normalized height after unloading

certain similarity in the trend and value. These results illustrate that the average deformation of mineral grains shows the same trend in the vertical direction. The mean value of the strain component ε_{zz} is mainly concentrated at approximately −0.025 and reaches the maximum value at the bottom of the sample. At the bottom of the sample, the grains bear the maximum compression.

Furthermore, in the range of the normalized height between 0.8 and 1, the main strain components of the mineral grains fluctuated greatly in value. This is due to the concentration of mineral grains near the fracture zone. The curve showed a maximum value at a normalized height of 0.9, which was mainly because the grains in the fault zone were fractured, as shown in Fig. 10. Therefore, the mineral grains in the fault zone are subjected to large plastic deformation and even fracture, resulting in a large stress concentration, and Fig. 9(b) shows the behavior of the mutations.

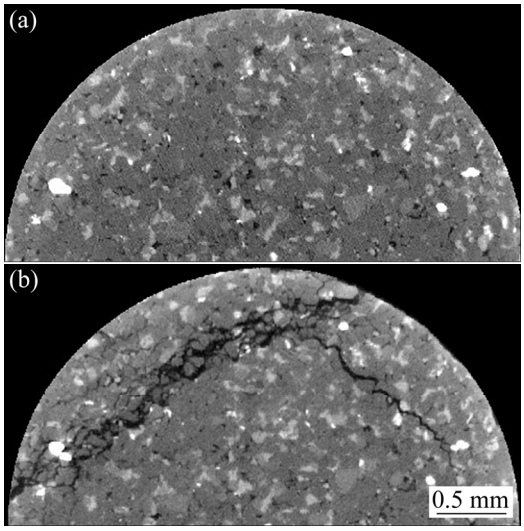

Fig. 10 Grayscale images at normalized height of 0.9: (a) Before loading; (b) After unloading

Figure 11 shows the spatial distribution of normal strain components. As shown in Fig. 11, normal strain components, ε_{xx}, ε_{yy} and ε_{zz}, range between −0.5 and 0.5 and are mainly concentrated between −0.1 and 0.1. This phenomenon of a large strain span is mainly reflected in the spatial distribution, namely, fault zones and nonfault zones.

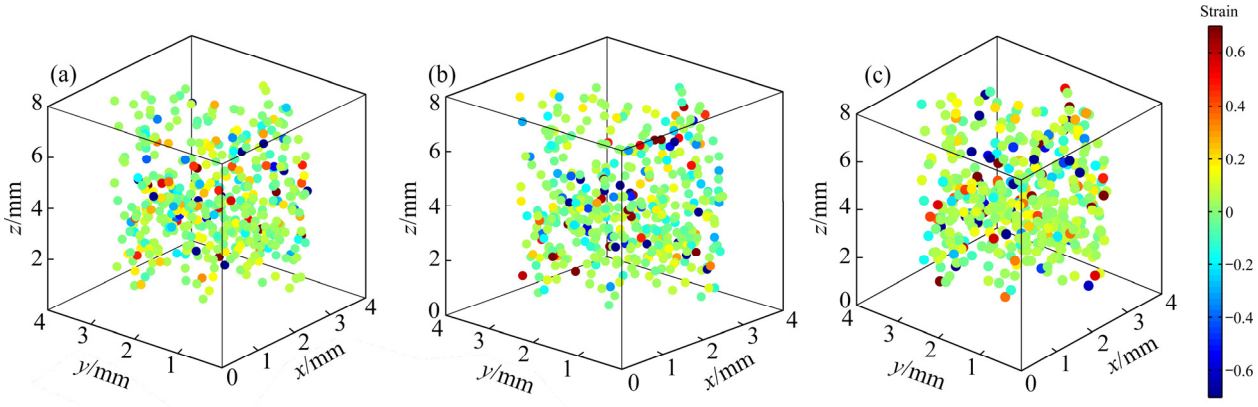

Fig. 11 Spatial distributions of normal strain components: (a) ε_{xx}; (b) ε_{yy}; (c) ε_{zz}

Figure 11 shows that the area with negative values means that the compression strain constitutes an inclined plane with an inclination angle of approximately 45°, which is the fault surface after compression, as shown in Fig. 12. After compression, the strain components in the fault zone were 5−10 times those in other areas, and the strain in the fault zone was mainly compression strain. Meanwhile, the strain components at the top of the sample were generally larger than those at the bottom of the sample. The samples showed compression deformation as a whole, among which the compression strain in the nonfault zone was mainly concentrated between 0 and 0.1 and that in the fault zone was mainly concentrated between −0.2 and −0.4. However, the strain behavior in the local area is shown as stretching, where the tensile strain value is concentrated at approximately 0.2.

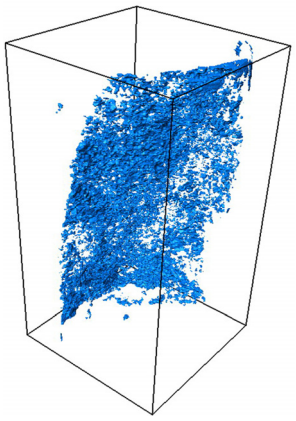

Fig. 12 Shape of fracture

3.3.3 Probability distribution of spatial stress and strain of mineral grains

Figure 13 shows the probability distribution of strain and stress. As shown in Fig. 13(c), the probability distribution of the sum of normal strain components mainly changes between −1.5 and 1.5. It is estimated that 70% of the strain is concentrated between −0.5 and 0.5, indicating that the sum of the normal strain components shows a wide range, and the strain distribution is relatively concentrated. However, the value of the strain is still different from the macroscopic strain of sandstone.

Figure 13(a) shows that the mean value of each normal strain component is 0.01, 0.13 and −0.17 for ε_{xx}, ε_{yy} and ε_{zz}, respectively. Figure 13(b) shows that the mean value of stress is 3.5, 23.2 and −32.3 MPa or σ_{xx}, σ_{yy} and σ_{zz}, respectively. The

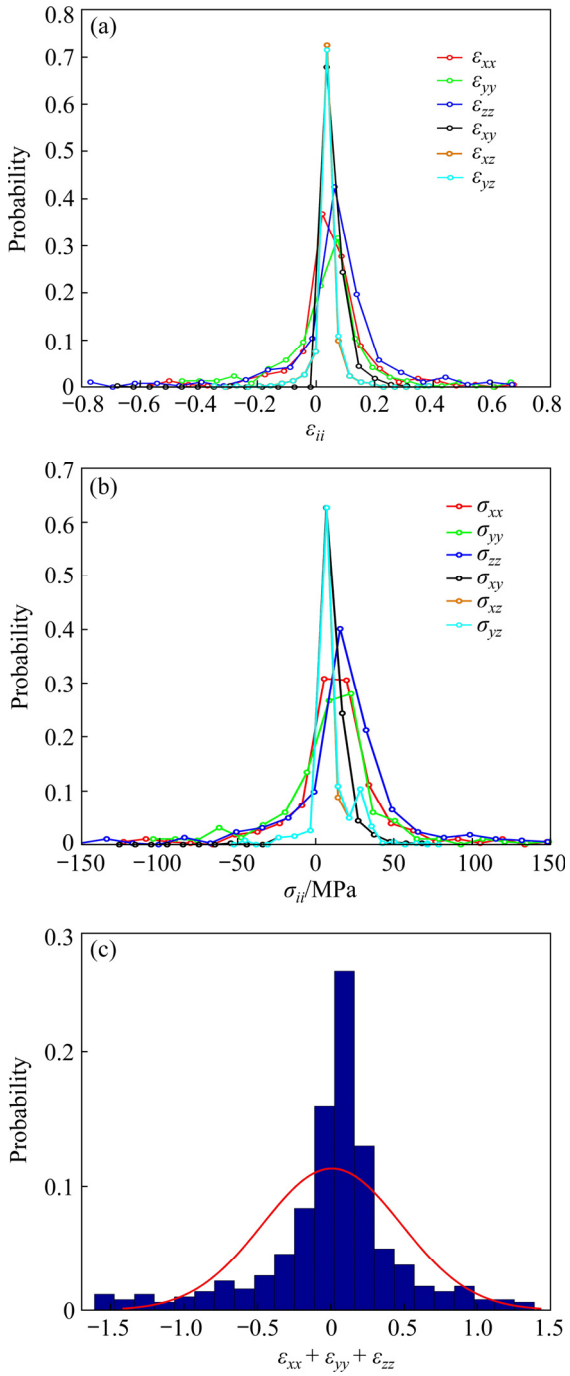

Fig. 13 Probability distributions of strain and stress: (a) Strain components; (b) Stress components; (c) Sum of strain components

variance of each normal strain component is 0.0014, 0.0054 and 0.0023 for ε_{xx}, ε_{yy} and ε_{zz}, respectively, and the variance of each stress component is 0.38, 1.20 and 0.54 for σ_{xx}, σ_{yy} and σ_{zz}, respectively. The stress components of mineral grains range from −100 to 100 MPa and are mainly concentrated between −20 and 30 MPa. Meanwhile, the strain components of the grains range from −0.6 to 0.6 and are mainly concentrated between −0.1 and 0.15.

After the uniaxial compression test, the uniaxial compressive strength of sandstone was calculated to be 30 MPa, the strain was 0.013, and the elastic modulus and Poisson's ratio were 0.23 GPa and 0.12, respectively.

Figure 13(b) shows the large stress on mineral grains after compression. The mean values of σ_{zz} are negative, and the mean values of σ_{xx} and σ_{yy} are positive, indicating that the grains were subjected to compressive stress in the *z*-axis and tensile stress in the *xy* plane. These results are consistent with Fig. 11.

Therefore, the strain of mineral grains is much larger than that of sandstone, and large plastic deformation can be found in sandstone. It is estimated that the plastic strain of the grains in the fault zone is approximately 30 times the macroscopic strain of sandstone and that of the grains in the nonfault zone is approximately 5 times the macroscopic strain of sandstone, indicating that the deformation of mineral grains is much larger than the macroscopic strain of sandstone.

3.4 Shear strain

In Sections 3.1 to 3.3, the deformation behavior of a single mineral grain after unloading was discussed. In this section, the deformation behavior of mineral grain aggregates, namely, grain clusters, was studied. Theoretically, shear deformation is decomposed into two additive parts: Green shear strain and Stokes local rotation [34]. For multicomponent sandstone, Green shear strain cannot be obtained because the mineral grains have varied shapes, sizes, and stochastic distributions. Hence, the material lines [34] are used to obtain the Stokes local rotation. To further observe the complex strain of the *xy* plane, the S−R decomposition theorem [35,36] in the Lagrange coordinate system is introduced to reveal the shear strain complexity in sandstone under uniaxial compression. Based on the principle of material invariance, we used material lines to characterize the element deformation, and acquired the shear strain contour map after fracture by tracing material lines inside the rock.

It has been pointed out that the constitutive equation of materials can be expressed as follows [36]:

$$\gamma=\frac{\tau}{G(1-\beta)} \tag{9}$$

where γ is the shear strain, β is the constitutive evolution parameter of the material which is related to the damage and stress state, G is the modulus of rigidity, and τ is the shear stress.

In S−R decomposition theory, the deformation tensor ($\boldsymbol{F}_j^i$) is expressed as the sum of strain tensor ($\boldsymbol{S}_j^i$) and rotation tensor ($\boldsymbol{R}_j^i$) as follows:

$$\boldsymbol{F}_j^i=\boldsymbol{S}_j^i+\boldsymbol{R}_j^i \tag{10}$$

3.4.1 Theory of material line construction on planar curves

For rock samples, if a material line is constructed along characteristic components, it is generally a curve. Before deformation, the material line (dS) is expressed as follows:

$$\mathrm{d}S=\left|\mathrm{d}S\right|\cdot[\cos(\alpha_0\boldsymbol{e}_1)+\sin(\alpha_0\boldsymbol{e}_2)] \tag{11}$$

where α_0 is the angle between the starting normal line and the ending normal line before deformation, $\boldsymbol{e}_1$ and $\boldsymbol{e}_2$ are the tangent vector and the normal vector of the unit length of the material line of the starting point, respectively. After deformation, this material line is expressed as follows:

$$\mathrm{d}S=\left|\mathrm{d}S\right|\cdot[\cos(\alpha\boldsymbol{e}_1)+\sin(\alpha\boldsymbol{e}_2)] \tag{12}$$

And the shear strain ω is represented as follows:

$$\omega=\frac{\alpha-\alpha_0}{\left|\mathrm{d}S_0\right|} \tag{13}$$

Equations (10)−(13) are used to practically measure tensile strain and shear strain due to the random distribution of the microstructure. Assuming a planar isotropic distribution, then we have S_{11}=S_{22}. Based on the experimental data, the mean area of Green strain is assumed to be reasonably zero, namely, $\varepsilon_{11}\approx\varepsilon_{22}\approx0$. Because of the independence of shear strain, these values can be discarded.

In the non-fracture zone, θ in Fig. 8(a) can be measured by the comparison of dS_0 and dS. $|\mathrm{d}S_0|$ is taken as the constant value, and $|\mathrm{d}S_0|$=1 is defined as the unit scale in global measurement. For the fracture zone, since a material line is broken into two staggered material lines, the theoretical formula is adopted as follows:

$$S_1^1=S_2^2=1-\cos\theta \tag{14}$$

where S_1 and S_2 are staggered material lines.

In mechanics, the residual shear strain in the

fracture zone is slightly smaller than the plastic shear strain in the non-fracture zone.

There are 352 and 364 material lines at two scales randomly selected on the CT slice. The middle point of the material line before the rock fracture is taken as the marker to draw the contour map of shear strain, as shown in Fig. 14. In Fig. 14, two curves are composed of five material points, and material lines are constructed using the right-hand rule. The basic principles of material line selection are as follows.

(1) The bending of the material line before and after deformation is unidirectional, and the length is greater than or equal to the selected unit length. The substance on the material line must be the same.

(2) When the material line is periodic, its length should be less than half of the spatial wavelength based on the sampling law.

(3) When material lines are randomly distributed and bent, continuous data on the plane should be guaranteed in the open covering of unit length.

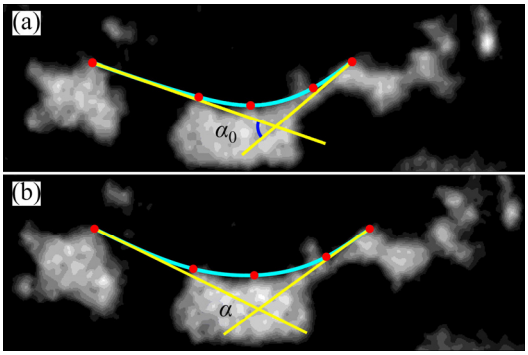

Fig. 14 Material line: (a) Before deformation; (b) After deformation

3.4.2 Contour map distribution of shear strain based on material line

Figure 15 shows contour maps of shear strain. Material lines are the proportional scale, and lines crossed the center of the circle are the starting lines for measuring shear strain. The shear strain was measured by two length scale lines, and the shear strain distribution was basically consistent. As shown in Fig. 15(a), the maximum shear strain is 0.65, and the minimum shear strain is −0.5. As shown in Fig. 15(b), the maximum shear strain is 0.35, and the minimum shear strain is −0.36.

However, in the sub-fracture zone, the contour maps of the two scales showed great differences.

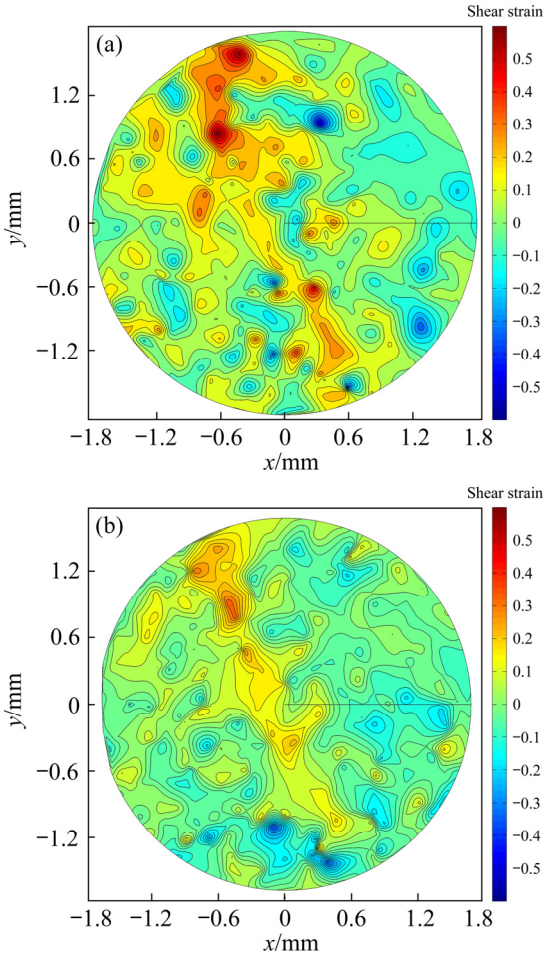

Fig. 15 Shear strain contour map: (a) Measured by using material line 1; (b) Measured by using material line 2

In Fig. 15(a), the critical residual shear strain is predicted by the contour map to be 0.5, whereas the strain of sandstone is 0.015. The shear strain in the fracture zone is greater than the compression strain of sandstone, so the mechanism of fracture shows strain concentration near the fracture zone, namely, shear concentration.

Then, near the main fracture, shear strain concentration occurs in the sandstone, and the strain value is proportional to the crack width. The shear strain distribution presents periodic changes, decreasing along the vertical direction of the main fracture and expending to both sides. In addition, at both ends of the main fracture, two approximately circular high shear strain zones are formed.

Furthermore, in the subcrack network, the strain state is complex, presenting a positive and negative interphase regional distribution. The shape and size of the strain islands are consistent with the grain size in the CT image after unloading. However, the map measured by the large-scale

material lines did not provide enough detailed information, as shown in Fig. 15(b), indicating that strain measurement is related to the selection of an appropriate measurement scale.

3.4.3 Shear strain profiles of contour map

To visualize numerical changes on the contour map of two scales and further explain the relationship between the periodic shear strain and its spatial position, the shear strain profiles at different angles (0°, 45°, 90°, 135°) were drawn counterclockwise at intervals of 45° by using the starting line to cut the contour map, as shown in Fig. 16. The results show that the shear strain distribution presents a periodic phenomenon of radial space. The value rises and falls periodically along the x-axis and presents an approximate symmetry along the y-axis. Four sets of curves are similar in shape. The profiles measured by the small-scale material lines can be divided into three regions, as shown in Figs. 16(a−d). Figure 17 shows the rotations and deformation of grain clusters in the three regions.

(1) Center circle: this region is distributed at shear strains of from −0.1 to 0.1, as shown in Fig. 16. Four sets of curves in Figs. 16(a−d), are similar in shape, range and value, corresponding to the red area in Fig. 17. The rotation of the central axis of mineral grains in the subfracture zone in this region can be explained by the grain rotation in Fig. 8(a), and the axial direction of quartz grains is marked by lines. In this area, quartz grains rotate and show symmetry along the subcrack zone, which

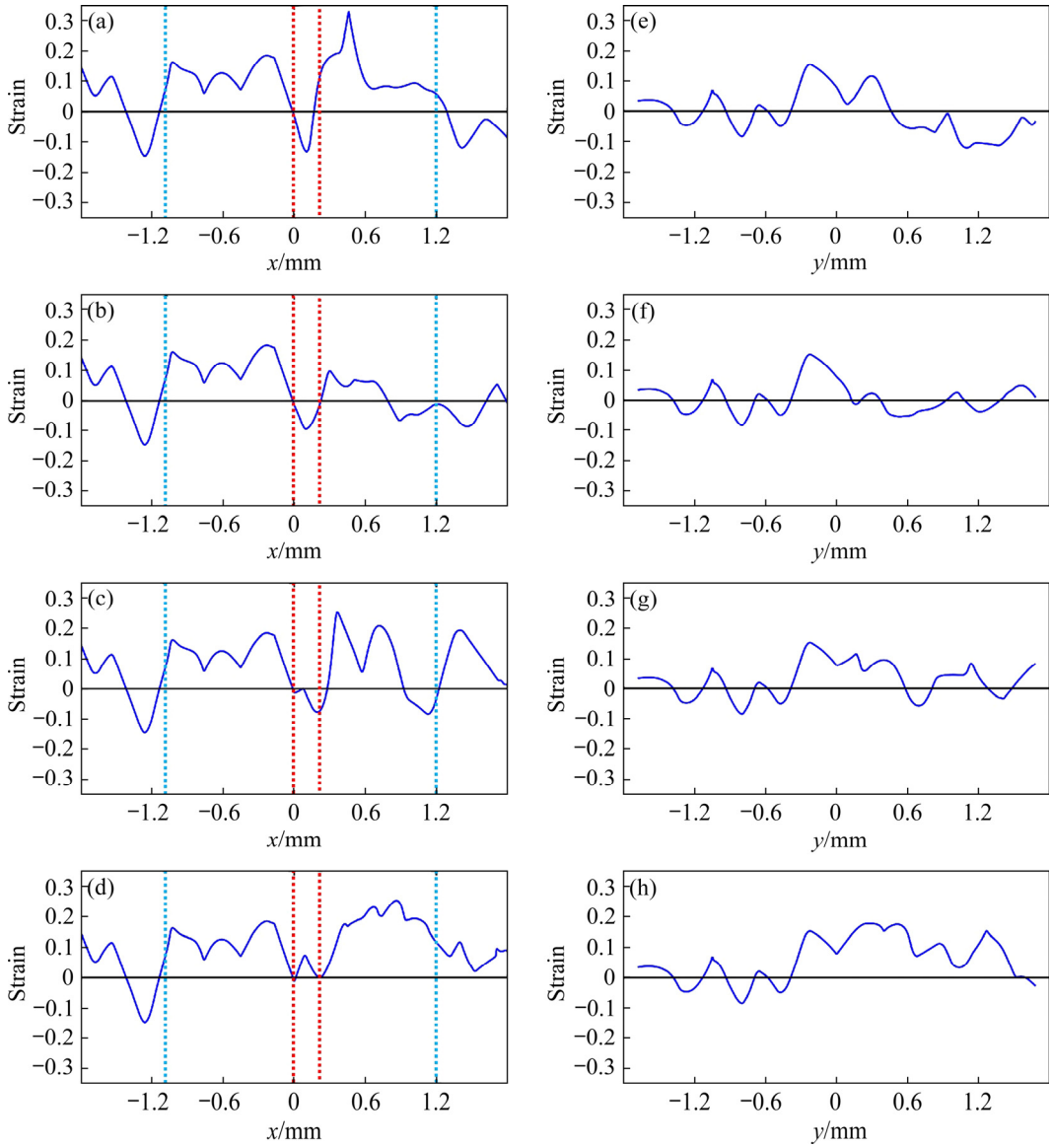

Fig. 16 Shear strain profiles at different angles relative to starting line: (a, e) 0°; (b, f) 45°; (c, g) 90°; (d, h) 135°

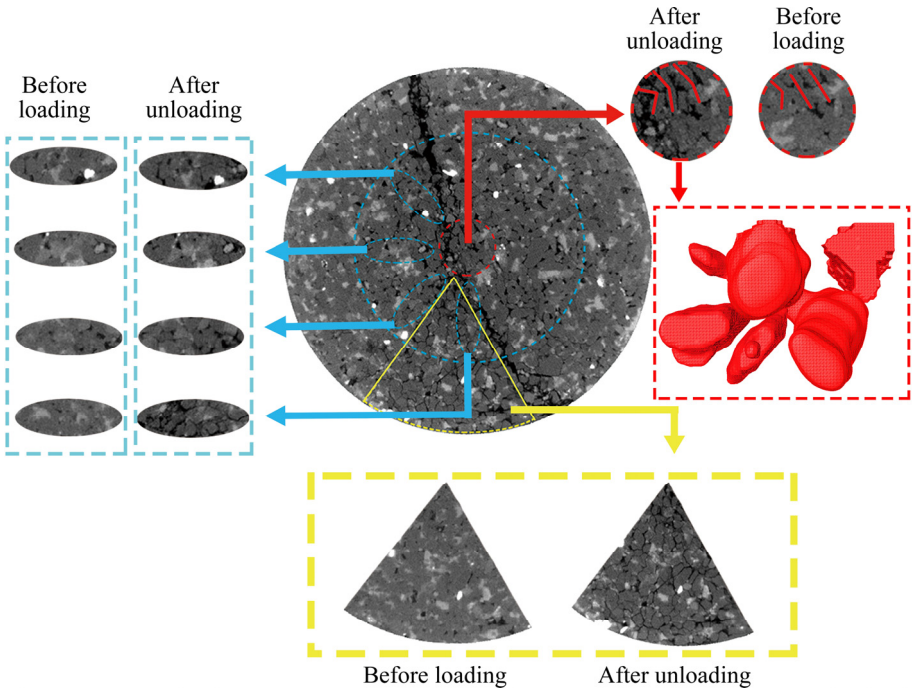

Fig. 17 Rotations and deformation of grain clusters in three regions

is similar to twins. The propagation and coalescence of microcracks are caused by the rotation of mineral grains.

(2) Middle ring: This region is distributed at shear strains between −0.2 and 0.2, as shown in Fig. 16, corresponding to the blue area in Fig. 17. Four sets of curves are similar in shape, but there are large differences in values and ranges. This is because the shear strain on the right side of the fault is smaller than that on the left side of the fault. The "M"-shaped curve in the figure is caused by the uneven rotation gradient of the cluster, as shown in Figs. 16(a−d), and the rotation of the grain cluster is shown in Fig. 17 (blue circles).

(3) Sandstone edge: This region is distributed at shear strains between −0.2 and 0.15, as shown in Fig. 16, corresponding to the rest of the area in Fig. 17. Four sets of curves have obvious differences in shape, range and value, and there is no obvious symmetry. In Fig. 15(b), the shear strain of the grain cluster in this region presents a positive and negative distribution, especially in the subfracture zone. This is due to the contrary rotation direction of the grain cluster during uniaxial compression, which results in the initiation, propagation and coalescence of cracks.

The shear strain measurement of CT slices by using two-scale material lines shows that the distribution of the rock deformation field is not uniform, and complex large deformation is measured by the small-scale material lines. Meanwhile, on the large scale, namely, the macroscale, the field can be regarded as a uniform deformation field and a simple small deformation. The problem of large deformation and small deformation discussed here depends on the size of the sample and the amount of deformation. The material line is used to measure the local rotation angle of the grain cluster inside the rock to overcome the error caused by the out-of-plane displacement of mineral grains. However, due to the problem of image accuracy and material point recognition rate, a certain error is caused, and the error cannot be estimated.

By measuring the local rotation angle of the material line, it is found that there is periodic strain distribution inside sandstone after unloading, and the residual strain is a cumulative process. After unloading, the residual shear strain still has a large value, indicating its irreversibility. Therefore, during the material fracture process, crack initiation and propagation are generated by irreversible local rotation angles, which are represented by rotation angle parameters and the direction of rotation. When the local rotation angle increases to the critical value, fracture will occur in the rotation direction. Meanwhile, for the micro local rotation angle, $\Theta(=\Theta_c\delta(x-x_0, y-y_0, z-z_0))$ inside the medium,

the point (x_0, y_0, z_0) is a singularity (fracture point or defect). In theory, this satisfies the equation of $\nabla^2\Theta=0$ (Laplace equation) in the elastic deformation zone Θ, presenting a circular fatigue striation centered on the singularity.

The results show that there is a characteristic deformation scale, L_0, determined by the microstructure of the material. When the scale $L \ll L_0$, or $L \gg L_0$, the shear strain is very small, and moreover, the periodic distribution of shear deformation in space shows that the characteristic deformation scale, L_0, is a half-period. The shear strain scale of the fatigue fracture deformation may be the key data for improving the microstructure of materials to improve the fatigue fracture resistance. For most fatigue and fracture, the maximum value of the local rotation angle is distributed in bands, corresponding to the shear failure zone in engineering.

4 Conclusions

(1) After unloading, mineral grains in the nonfault zone move radially outward, while the volume of mineral grains decreases along its maximum principal axis, and the sphericity increases. The deformation of mineral grains in the fault zone is large, and their volumes increase. The internal grains of the sandstone exhibit complex stress states and deformation behaviors.

(2) There are significant differences in the deformation behavior of grains between the fracture zone and the nonfracture zone. The grain strain components ε_{xx} and ε_{yy} are significantly smaller than ε_{zz}, and the fluctuation degrees of ε_{xx} and ε_{yy} are less than that of ε_{zz}. Grains are subjected to compressive stress in the z-axis direction and tensile stress in the xy plane. The grain strains in the fracture zone and non-fracture zone are approximately 30 and 5 times the macrostrain of the sample, respectively, which indicates that there is a significant difference in the deformation behavior between the grains and the macroscopic sample.

(3) The shear and strain profiles are plotted. There is a near-periodic shear strain distribution phenomenon in the radial direction. The shear strain near the fault zone is obviously larger than the compressive strain. This shows that the basic mechanism of fracture is the shear stress concentration near the fracture zone. During the material fracture process, the initiation and propagation of cracks are caused by irreversible local rotation angles. When the local rotation angle increases to the critical value, cracks will occur in the rotation direction.

Acknowledgments

This work was financially supported in part by the National Key Research and Development Program of China (No. 2017YFC0602901).

References

[1] LONG Yi, LIU Jian-po, LEI Gang, SI Ying-tao, ZHANG Chang-yin, WEI Deng-cheng, SHI Hong-xu. Progressive fracture processes around tunnel triggered by blast disturbances under biaxial compression with different lateral pressure coefficients [J]. Transactions of Nonferrous Metals Society of China, 2020, 30(9): 2518−2535.

[2] LI Xi-bing, CHEN Zheng-hong, WENG Lei, LI Chong-jin. Unloading responses of pre-flawed rock specimens under different unloading rates [J]. Transactions of Nonferrous Metals Society of China, 2019, 29(7): 1516−1526.

[3] XIE C Y, NGUYEN H N Y, BUI X N, NGUYEN V T, ZHOU J. Predicting roof displacement of roadways in underground coal mines using adaptive neuro-fuzzy inference system optimized by various physics-based optimization algorithms [J]. Journal of Rock Mechanics and Geotechnical Engineering, 2021, 13(6): 1452−1465.

[4] SHANG J L, WEST L J, HENCHER S R, ZHAO Z Y. Geological discontinuity persistence: Implications and quantification [J]. Engineering Geology, 2018, 241: 41−54.

[5] SHANG Jun-long. Rupture of veined granite in polyaxial compression: insights from three-dimensional discrete element method modeling [J]. Journal of Geophysical Research: Solid Earth, 2020, 125(2): e2019JB019052.

[6] PUTNIS A, MAUTHE G. The effect of pore size on cementation in porous rocks [J]. Geofluids, 2001, 1(1): 37−41.

[7] LI X Q, LIN C L, MILLER J D, JOHNSON W P. Pore-scale observation of microsphere deposition at grain-to-grain contacts over assemblage-scale porous media domains using X-ray microtomography [J]. Environmental Science & Technology, 2006, 40(12): 3762−3768.

[8] MADADI M, SAADATFAR M. A finite-element study of the influence of grain contacts on the elastic properties of unconsolidated sandstones [J]. International Journal of Rock Mechanics and Mining sciences, 2017, 93: 226−233.

[9] LI Q Y, TULLIS T E, GOLDSBY D, CARPICK R W. Frictional ageing from interfacial bonding and the origins of rate and state friction [J]. Nature, 2011, 480(7376): 233−236.

[10] VERBERNE B A, PLÜMPER O, de WINTER D A M, SPIERS C J. Rock mechanism: Superplastic nanofibrous slip zones control seismogenic fault friction [J]. Science, 2014, 346(6215): 1342−1344.

[11] BOBYLEV S V, OVID′KO I A. Grain boundary rotations in solids [J]. Physical Review Letters, 2012, 109(17): 175501.

[12] COTTERELL B, RICE J R. Slightly curved or kinked cracks [J]. International Journal of Fracture, 1980, 16(2): 155−169.

[13] LIN Qing, BIAN Xin, PAN Peng-zhi, GAO Yue, LU Yun-hu. Criterion of local symmetry visualized in small eccentric single edge notched bend (E-SENB) rock specimens [J]. Engineering Fracture Mechanics, 2021, 248: 107709.

[14] RÖNTGEN M, MORFONIOS C V, WANG R, dal NEGRO L, SCHMELCHER P. Local symmetry theory of resonator structures for the real-space control of edge states in binary aperiodic chains [J]. Physical Review B, 2019, 99(21): 214201.

[15] BAI Xin, ZHANG Dong-ming, ZENG Sheng, ZHANG Shu-wen, WANG Deng-ke, WANG Fu-lin. An enhanced coalbed methane recovery technique based on CO_2 phase transition jet coal breaking behavior [J]. Fuel, 2020, 265: 116912.

[16] LIANG Chang-yu, WU Shu-ren, LI Xiao. Research on micro-meso characteristics of granite fracture under uniaxial compression at low and intermediate strain rates [J]. Chinese Journal of Rock Mechanics and Engineering, 2015, 34(S1): 2977−2986. (in Chinese)

[17] HURLEY R C, LIND J, PAGAN D C, AKIN M C, HERBOLD E B. In situ grain fracture mechanics during uniaxial compaction of granular solids [J]. Journal of Mechanics and Physics of Solids, 2018, 112: 273−290.

[18] SIBSON R H. Earthquakes and rock deformation in crustal fault zones [J]. Annual Review of Earth and Planetary Sciences, 1986, 14(1): 149−175.

[19] HURLEY R C, HALL S A, WRIGHT J P. Multi-scale mechanics of granular solids from grain-resolved X-ray measurements [J]. Proceedings of Royal Society A — Mathematical, Physical, and Engineering Sciences, 2017, 473(2207): 20170491.

[20] HURLEY R C, LIND J, PAGAN D C, HOMEL M A, AKIN M C, HERBOLD E B. Linking initial microstructure and local response during quasistatic granular compaction [J]. Physical Review E, 2017, 96(1): 012905.

[21] LAN Heng-xing, MARTIN C D, HU Bo. Effect of heterogeneity of brittle rock on micromechanical extensile behavior during compression loading [J]. Journal of Geophysical Research: Solid Earth, 2010, 115(B1): B01202.

[22] KOCK I, HUHN K. Influence of particle shape on the frictional strength of sediments—A numerical case study [J]. Sedimentary Geology, 2007, 196(1−4): 217−233.

[23] LIU Guang, RONG Guan, PENG Jun, HOU Di, ZHOU Chuang-bing. Mechanical behaviors of rock affected by mineral particle shapes [J]. Chinese Journal of Geotechnical Engineering, 2013, 35(3): 540−550. (in Chinese)

[24] SUNDARAM B M, TIPPUR H V. Full-field measurement of contact-point and crack-tip deformations in soda-lime glass. Part II: Stress wave loading [J]. International Journal of Applied Glass Science, 2018, 9(1): 123−136.

[25] TAN H, LIU C, HUANG Y, GEUBELLE P H. The cohesive law for the particle/matrix interfaces in high explosives [J]. Journal of the Mechanics and Physics of Solids, 2005, 53(8): 1892−1917.

[26] MARUYAMA G, HIRAGA T. Grain- to multiple-grain-scale deformation processes during diffusion creep of forsterite + diopside aggregate: 1. Direct observations [J]. Journal of Geophysical Research: Solid Earth, 2017, 122(8): 5890−5915.

[27] DONG Yan-long, CAO Shu-yun, CHENG Xue-mei, LIU Jun-lai, CAO Han-chen. Grain-size reduction of feldspar and flow of deformed granites within the Gaoligong shear zone southwestern Yunnan, China [J]. Science China Earth Sciences, 2019, 62(9): 1379−1398.

[28] TING J M, MEACHUM L, ROWELL J D. Effect of particle shape on the strength and deformation mechanisms of ellipse-shaped granular assemblages [J]. Engineering Computations, 1995, 12(2): 99−108.

[29] PRATT W K. Digital Image Processing [M]. New York: Wiley and Sons. 1978.

[30] HURLEY R C, HERBOLD E B, PAGAN D C. Characterization of the crystal structure, kinematics, stresses and rotations in angular granular quartz during compaction [J]. Journal of Applied Crystallography, 2018, 51(4): 1021−1034.

[31] ZHANG Yan-qiu, JIANG Shu-yong. Molecular dynamics simulation on mechanisms of plastic anisotropy in nanotwinned polycrystalline copper with {111} texture during tensile deformation [J]. Transactions of Nonferrous Metals Society of China, 2021, 31(5): 1381−1396.

[32] COUTINHO Y A, ROONEY S C K, PAYTON E J. Analysis of EBSD grain size measurements using microstructure simulations and a customizable pattern matching library for grain perimeter estimation [J]. Metallurgical and Materials Transactions A—Physical Metallurgy and Materials Science, 2017, 48(5): 2375−2395.

[33] KALO K, GRGIC D, AUVRAY C, GIRAUD A, DRACH B, SEVOSTIANOV I. Effective elastic moduli of a heterogeneous oolitic rock containing 3-D irregularly shaped pores [J]. International Journal of Rock Mechanics and Mining Sciences, 2017, 98: 20−32.

[34] XIAO J. Strain geometric field theory [M]. Beijing: China Science Publishing & Media Ltd, 2017. (in Chinese)

[35] GAO Ya-nan, YAN Wei-cheng, GAO Feng, WANG Ze-kai, ZHANG Zhi-zhen. Study on mechanical properties and finite deformation constitutive model of red sandstone subjected to temperature–water-mechanics coupling [J]. Chinese Journal of Rock Mechanics and Engineering, 2019, 38(s1): 2734−2747. (in Chinese)

[36] CHEN Zhi-da. Rational mechanics [M]. Chongqing: Chongqing Publishing House, 2000. (in Chinese)

基于 XCT 扫描的砂岩矿物颗粒微尺度变形行为

秦亚光[1,2]，古德生[2]，胡建华[2]，杨东杰[2]，马少维[2]，白 鑫[3]，冯春迪[2]

1. 中国电建集团 华东勘测设计研究院有限公司，杭州 311122；
2. 中南大学 资源与安全工程学院，长沙 410083；
3. 南华大学 资源环境与安全工程学院，衡阳 421000

摘 要：为了定量表征岩石中三维微结构在单轴压缩下的物理和力学行为，采用高精度原位计算机断层扫描技术研究砂岩矿物颗粒运动、旋转变形和主应变特性，揭示断裂带与非断裂带之间的晶粒行为。结果表明：卸载后，矿物颗粒的剪切应变在径向呈现周期性变化；断裂带和非断裂带区域内部颗粒应变分别约为试样宏观应变的 30 和 5 倍；断裂带区域附近的剪切应变大于压缩应变，且呈剪应力集中的特征。

关键词：颗粒变形；原位 XCT；失效行为；斯托克斯旋转；物质线

(Edited by Wei-ping CHEN)